Journal of Aerosol Science 157 (2021) 105820

Contents lists available at ScienceDirect

Journal of Aerosol Science

journal homepage: www.elsevier.com/locate/jaerosci

Coated soot particles with tunable, well-controlled properties generated in the laboratory with a miniCAST BC and a micro smog chamber

Michaela N. Ess [a], Michele Bertò [b], Alejandro Keller [c], Martin Gysel-Beer [b], Konstantina Vasilatou [a,*]

[a] Federal Institute of Metrology METAS, Bern-Wabern, Switzerland
[b] Laboratory Atmospheric Chemistry, Paul Scherrer Institute, 5232, Villigen, Switzerland
[c] University of Applied Sciences Northwestern Switzerland, 5210, Windisch, Switzerland

ARTICLE INFO

Keywords:
Soot
Coating
Secondary organic matter
Micro smog chamber
Calibration aerosol

ABSTRACT

A Micro Smog Chamber (MSC) was coupled for the first time with a miniCAST 5201 Type BC combustion generator with the aim to produce a series of stable and reproducible model aerosols simulating the physical properties of combustion particles present in ambient air. With this setup it was possible to generate particles ranging from "fresh" soot (single scattering albedo $SSA \leq 0.05$, absorption Ångström exponent *AAE* close to 1, high EC/TC mass fraction (approximately 90%) and mobility diameter typically <100 nm) to "aged" soot with different amounts of organic coating. The "aged" soot particles could grow up to 200 nm and exhibited high *SSA* (up to 0.7 at $\lambda = 870$ nm), an increased *AAE* (up to 1.7) and low EC/TC mass fraction (down to <10%). The ageing was achieved by coating the soot particles with increasing amounts of secondary organic matter (SOM) formed by the photo-oxidation of α-pinene or mesitylene in the MSC. Thereby, the *SSA* and *AAE* increased with coating thickness, while the EC/TC mass fraction decreased. Over the experimental period of 2 h, the generation of the "aged" soot aerosols was stable with a standard deviation in particle size and number concentration of <1% and <6%, respectively. The day-to-day reproducibility was also satisfactory: with α-pinene as SOM precursor the variability (standard deviation) in particle size was <2% and in the *AAE* and *SSA* < 6%. Particle number concentrations up to 10^6 cm^{-3} and mass concentrations up to 15 mg/m^3 (depending on particle size and SOM amount) could be generated, much higher than what has been reported with other oxidation flow reactors. The generated carbonaceous aerosols could find useful applications in the field of aerosol instrument calibration, particularly in the standardization of filter-based absorption photometers under controlled conditions.

1. Introduction

Black carbon (BC), soot and elemental carbon (EC) describe particulate carbonaceous substances with strong light absorption properties. Soot describes carbonaceous particles that are formed by incomplete combustion processes of biomass and fossil fuels

* Corresponding author. Laboratory Particles and Aerosols, Federal Institute of Metrology METAS, Lindenweg 50, 3003, Wabern-Bern, Switzerland.
E-mail address: Konstantina.Vasilatou@metas.ch (K. Vasilatou).

https://doi.org/10.1016/j.jaerosci.2021.105820
Received 19 February 2021; Received in revised form 7 May 2021; Accepted 8 May 2021
Available online 28 May 2021

(Penner et al., 2001), while BC and EC are qualitative names for quite similar subsets of carbonaceous materials identified using different experimental methods (Buseck, Adachi, Gelencsér, Tompa, & Pósfai, 2012; Petzold et al., 2013). Thermo-optical methods are used to discriminate between elemental carbon (EC) and organic carbon (OC) (Joel C. Corbin et al., 2020). EC is thereby the carbonaceous material that is refractory and can only be oxidized at high temperatures (Ogren & Charlson, 1983; Petzold et al., 2013), compared to OC that gasifies in inert gas. BC is defined as highly graphitized carbonaceous material (soot BC consisting of aggregate particles and char BC consisting of large cenospheres (J. C. Corbin et al., 2019)) showing strong visible light absorption, high mass absorption coefficient (MAC) of at least 5 m^2/g (at $\lambda = 550$ nm), which is refractory, insoluble in water and organic solvents, and contains a high sp^2-bonded carbon fraction (Bond et al., 2013; Petzold et al., 2013). BC in atmospheric aerosols is not a precisely defined material. Instead, it covers a certain range of degrees of graphitization and optical properties, starting with the continuous transition of brown carbon to BC to the conceptual defined highly ordered material (Bond et al., 2013; Joel C.; Corbin et al., 2020; Saleh, Cheng, & Atwi, 2018). Furthermore, no method exists to unambiguously and accurately quantify it. Therefore, it has been recommended by Petzold et al. (Petzold et al., 2013) to report operationally defined quantities depending on the method applied to quantify BC, e.g. equivalent BC (eBC) when data are obtained from optical absorption methods, and provide the MAC values which were used for inferring the eBC mass concentration from the measured aerosol light absorption coefficient.

Monitoring of carbonaceous particles in ambient air is essential due to their effects on climate and human health. To this end, filter-based absorption photometers have been used extensively since the 1980s at various monitoring stations worldwide. These instruments are compact, robust and suitable for unattended operation in the field, however they suffer from several measurement artefacts due to the use of filters for collecting the particles (McMurry, 2000). Although correction algorithms have been proposed for minimizing measurement biases (Collaud Coen et al., 2010; Virkkula, 2010; E.; Weingartner et al., 2003), deriving accurate and reliable information on aerosol properties, such as absorption coefficient or eBC mass concentration, is still challenging.

To investigate the performance of individual absorption photometers over time or to study unit-to-unit variability, several field intercomparison campaigns have been carried out (Cappa, Lack, Burkholder, & Ravishankara, 2008; Müller et al., 2011; Schmid et al., 2006). These show a large variation in the response to absorbing atmospheric aerosol particles depending on instrument type (Müller et al., 2011) and on the amount of non-BC material (e.g. non absorbing organic aerosol) present in the aerosol (Cappa et al., 2008, 2012). The unit-to-unit variability between instruments can reach 30% for particle soot absorption photometers (PSAPs) and aethalometers, while staying below 5% for multi-angle absorption photometers (MAAP) (Müller et al., 2011). Furthermore, measurements with non-absorbing particles showed that the current corrections for the cross sensitivity to particle scattering are not sufficient (Müller et al., 2011).

As an alternative to time-consuming and expensive field campaigns, smog-chamber experiments have been proposed for challenging absorption photometers with defined synthetic aerosols (Cappa et al., 2008; Saathoff et al., 2003a; E.; Weingartner et al., 2003). In this case, soot particles are typically coated with ozonolysis products of α-pinene to simulate atmospheric ageing processes (Schnaiter et al., 2005). Even though smog-chamber experiments are much more time and cost efficient than field campaigns, the time scales still remain long and range up to a few days for each measurement (E. Weingartner et al., 2003). As a result, such experiments are usually limited to the generation of a single or a limited number of test aerosols. A reliable calibration of absorption photometers with a series of different ambient-like lab-generated aerosols would not be applicable with smog-chambers in a reasonable time frame.

In recent years, oxidation flow reactors (OFR) are increasingly being used to study, among others, secondary organic aerosol (SOA) formation in the laboratory (Ahlberg et al., 2017; Bruns et al., 2015; Kang, Root, Toohey, & Brune, 2007; A. T.; Lambe, Chhabra, et al., 2015; A. T.; Lambe, Onasch, et al., 2011), investigate the morphological transformation of soot upon ageing (Pei et al., 2018) or determine soot properties as cloud condensation nuclei after oxidative processing (A. T. Lambe, Ahern, et al., 2015). Compared to smog chambers, OFRs offer the advantages that they are compact and easy to use and that the generation of SOA or the coating of particles with secondary organic matter (SOM) requires only a few seconds or minutes due to the small size of the reactor and the high UV radiation power. Several types of small reactor chambers with a residence time in the order of a few minutes or less have been reported in the literature (George, Vlasenko, Slowik, Broekhuizen, & Abbatt, 2007; Kang et al., 2007; Keller & Burtscher, 2012; A. T. Lambe, Ahern, et al., 2011, 2015). Most of these reactors have been designed, however, for oxidizing low concentrations of volatile organic materials (i.e. a few hundred ppb), such as those found in the atmosphere. Moreover, additional coating of soot particles with sulfuric acid might be needed to provide active acidic surfaces for the condensation of semi volatile SOM (from limonene ozonolysis) to increase the soot coating thickness to achieve diameter growth factors of the particles up to 2 (Pei et al., 2018).

Whereas past studies involving OFRs have focused on simulating atmospheric procedures as close as possible and studying oxidation reaction pathways in ambient air, the goal of this investigation was to generate a series of stable, reproducible test aerosols with atmospherically relevant physical/optical properties and EC/TC mass fractions to challenge common aerosol instruments. For this purpose, it is necessary to use a simple, compact and robust laboratory setup, which can be easily standardized. Moreover, it is essential to generate high aerosol flows (or, alternatively, high aerosol concentrations which can be diluted) in order to be able to test different instruments in parallel. One OFR fulfilling these requirements is known as micro smog chamber (MSC). The MSC was developed for studying the SOM potential of wood burning emissions and has therefore been optimized to operate at high particle concentrations (Keller & Burtscher, 2012). It has been shown that the MSC generates SOM of realistic chemical composition with yields within the range expected from previous smog-chamber studies (Bruns et al., 2015). So far, the application of the MSC has been limited, however, to firing installations (Bruns et al., 2015; Joel C.; Corbin, Keller, et al., 2015; Joel C.; Corbin, Lohmann, et al., 2015; Keller & Burtscher, 2012).

In this work, the MSC was coupled for the first time with a miniCAST combustion generator (Ess et al., 2021; Ess & Vasilatou, 2019) for controlled laboratory soot coating experiments to produce aged soot particles with similar sizes and optical properties as those present in the atmosphere. α-pinene, the most abundant monoterpene in the atmosphere (Simon et al., 2020), and mesitylene (1,3,

5-trimethylbenzene), a known aromatic compound emitted by fuel combustion (Baltensperger et al., 2005), were chosen as surrogate precursor gases for SOM production, representing biogenic and anthropogenic volatile organic compounds (VOCs), respectively. Soot particles of different sizes were tested as seed particles. A series of test aerosols simulating a large range of optical properties and EC/TC mass fractions could be generated and was characterized with respect to physical (particle size, mass concentration, effective density), optical (absorption Ångström exponent, single scattering albedo) and chemical (elemental carbon to total carbon EC/TC mass fraction) properties. Additionally, the stability and reproducibility of the aerosol generation was examined. Thus, a method for the controlled production of ambient-like carbonaceous aerosols (Bambha, Dansson, Schrader, & Michelsen, 2013; Lefevre, Yon, Liu, & Coppallea, 2018; Zhang et al., 2008) which can be standardized and find application in the calibration of common aerosol instrumentation is presented.

2. Experimental

2.1. Aerosol generation

A schematic representation of the aerosol generation setup is depicted in Fig. 1. Soot particles were generated with a miniCAST 5201 Type BC (Jing Ltd., Switzerland) as described in detail in Ess et al. (Ess et al., 2021; Ess & Vasilatou, 2019). Briefly, the miniCAST was mainly operated in the "premixed flame mode" under overall slightly fuel-lean conditions in order to maximize the EC/TC mass fraction of the soot particles. For the operation points "90 nm" to "100 nm" the gas flows were 0.06 L/min propane, 1.3 L/min oxidation air and 0.225 to 0.220 L/min mixing air, respectively. For the operation point "112 nm" the miniCAST was operated with 0.061 L/min propane, 1.5 L/min oxidation air and 0.085 L/min mixing air. Gas flows and particle properties for all operation points used can be found in the supporting information (section S1). After drying, the aerosol was diluted 1:10 with dry particle-free air (VKL 10 dilution unit, Palas GmbH, Germany), which resulted in 5% relative humidity (RH). For the experiments at increased humidity, the aerosol was passed through a commercial dryer used as humidifier (MD-700-12S-11, Permapure, Lakewood, USA) in combination with a cryothermostat (LAUDA Ecoline Staredition RE 306, LAUDA DR. R. WOBSER GMBH & CO. KG, Germany) resulting in RH that could be adjusted with high stability between 36% and 75% (depending on the cryothermostat's temperature). For the first proof-of-concept

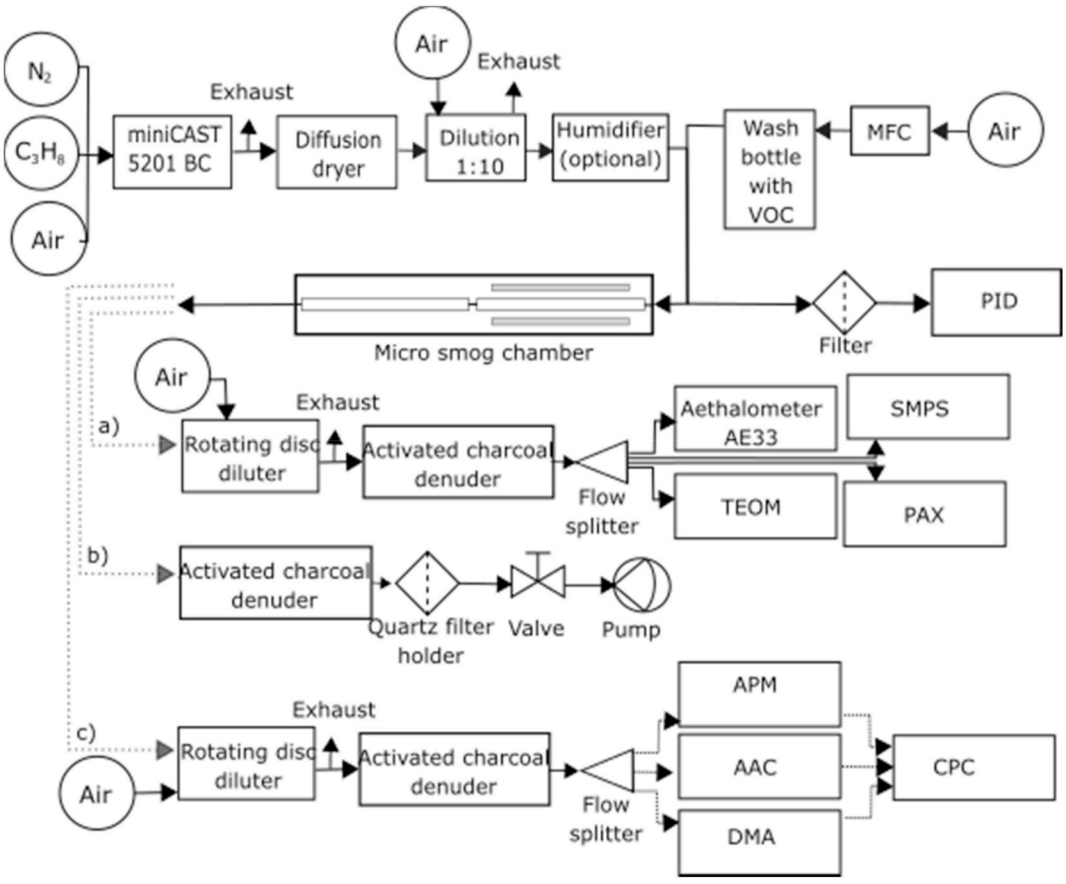

Fig. 1. Schematic illustration of the experimental setup. Path a) was used for general aerosol characterization, b) for filter sampling and c) for determining the effective density and comparing aerodynamic and mobility diameter.

experiments shown in the SI a custom-made Nafion humidifier was used. The aerosol humidity was measured right before the MSC with a digital humidity sensor (FHAD 46 series/Almemo D6, Ahlborn, Germany).

The soot was then mixed with a volatile organic compound (VOC; i.e. gas-phase SOM-precursor) in the micro smog chamber (MSC, model with 2 quartz tubes) (Keller & Burtscher, 2012). α-pinene (≥97% purity, Sigma Aldrich, Switzerland) or mesitylene (98% purity, Sigma Aldrich, Switzerland) were used as surrogates of biogenic and anthropogenic SOM precursor gases, respectively. A gas bubbler was used as VOC container. The VOC concentration in the soot-VOC-mixture was controlled by adjusting the flow of zero air through the gas bubbler with a mass flow controller (V-red-y Compact with hand valve, 1–100 mL/min, Vögtlin, Switzerland). The amount of VOC in the bubbler was kept low enough so as not to touch the lower tip of the internal glass tube which delivers the air. As a result, the air was delivered above the liquid surface, i.e. without bubbling through the α-pinene or mesitylene. Due to saturation and equilibration processes, the VOC concentration increased slowly with time at a constant air flow. The latter had to be regularly reduced to achieve a stable VOC concentration in the soot-VOC mixture entering the MSC. The gaseous concentration of the VOC in the mixture was determined with a photoionization detector (PID PhoCheck TIGER, Ion Science Ltd, UK) after filtering out the particles. To avoid long-term drifts in the VOC detection, the photoionization detector was calibrated with zero air and isobutylene (100 ppm isobutylene in air, Industrial Scientific, USA) on a daily basis.

In the MSC (Keller & Burtscher, 2012), the α-pinene or mesitylene vapors were oxidized by O_3 and/or OH radicals yielding secondary organic matter (SOM), part of which condensed on the soot particles as coating. Up to five low pressure mercury lamps (4 W UVC with 254 nm and 185 nm emission lines, type GPH212T5VH/2, Heraeus, Germany) surrounding the first cylindrical quartz chamber (0.25 m length, 0.02 m diameter, 76 mL volume) of the MSC can be used for O_3 and/or OH generation. The concentration of O_3 was measured with an ozone analyzer (Model 202, 2 B Technologies, USA) in the absence of particles and organic vapors at a constant flow rate of 1.2 L/min. When in operation, the UVC lamps heat the inside of the MSC to about 70 °C. Unless otherwise stated, four lamps were used during the experiments leading to a maximum O_3 concentration of 120 mg/m^3. The ozone concentration was stable during 6 h of continuous operation (standard deviation $< 1.6\%$) and the day-to-day reproducibility was also good (standard deviation $< 2.2\%$). The UVA lamp located above the second quartz chamber (same dimensions as the first) in the MSC was never used, so that this volume was a dark reaction volume before diluting the generated aerosol. Experiments with α-pinene took place under dry conditions (5% RH), where oxidation is dominated by O_3 radicals. On the contrary, experiments with mesitylene were performed at 37–40% RH, where oxidation occurs predominantly through OH radicals. At an aerosol flow rate of 1.2 L/min the average residence time of the particles in the MSC was calculated to be approximately 7.6 s, with 3.8 s residence time in each one of the quartz chambers.

Wavelengths from a mercury lamp (185 nm and 254 nm emission lines) have been shown by Nishida et al. (Nishida, Johnson, Boies, & Hochgreb, 2019) to charge soot unipolarly. Nevertheless, their setup uses a precipitation voltage during UV exposure to avoid recombination of negative ions with charged particles. Burtcher et al. (Burtcher et al., 1988) showed that photoelectric charging is very inefficient for setups without mitigation measures, like the precipitation voltage, and particle concentrations similar to the ones from our study. They also showed that coating with organic substances prevents photoemission to happen in the first place. Based on these results, we believe that charging in the MSC will be quenched due to SOM coating applied to the particles and the high recombination rate of ions produced by photoemission with the charged particles, but this assumption should be investigated in future work.

2.2. Particle monitoring and characterization

For general characterization, the aerosol was diluted with a rotating disc diluter (MD19-1i, Matter Engineering, Switzerland) right after the MSC. The rotating disc diluter ensured also a constant flow through the MSC and exchanged the gas phase with dry filtered ambient air, thus reducing VOCs and water from the aerosol. After passing through a denuder filled with activated charcoal to remove residual gas-phase organics (if still present) and a silica gel diffusion dryer, the aerosol was split in up to four portions and delivered to a scanning mobility particle sizer (SMPS + C with L-DMA (Am-241 neutralizer) and CPC model 5.403, Grimm Aerosol Technik GmbH & Co. KG, Germany), an aethalometer (AE33 Aethalometer, Magee Scientific, USA), a photoacoustic extinctiometer (PAX, 870 nm wavelength, Droplet Measurement Technologies, USA) and a tapered element oscillating microbalance (TEOM 1405, Thermo Scientific, USA), as shown in path a) of Fig. 1).

The particle size distribution was determined with the SMPS in stepping mode. The manufacturer's software (Nano V1-5-3, Grimm Aerosol Technik GmbH & Co. KG, Germany) was applied to infer the number size distribution in terms of mobility diameter. The column was suitable for particles with mobility diameter between 11 nm and 1050 nm. The ratio of the DMA sheath air to the aerosol flow was 10:1 with aerosol and sheath air flow set to 0.3 L/min and 3 L/min, respectively. The resolution was set to 45 channels and every measurement was repeated at least three times. The aerosol total mass concentration was measured with the TEOM, operated at a flow rate of 1 L/min and a temperature of 30 °C to reduce artefacts due to the evaporation of semi-volatile organic material. The raw frequency of the TEOM mass transducer was recorded via a custom-made LabVIEW routine every 6 s without averaging and the aerosol mass concentration m_c was calculated according to equation (1). Here, Δm_{Filter} denotes the change of the particle mass on the TEOM filter during the measurement time Δt, $\dot{V}$ the flow rate, K_0 the calibration constant of the mass transducer and f its frequency.

$$m_c = \frac{\Delta m_{Filter}}{\Delta t} \cdot \frac{1}{\dot{V}} = \frac{K_0 \left(\frac{1}{f_{i+1}^2} - \frac{1}{f_i^2} \right)}{\Delta t} \cdot \frac{1}{\dot{V}} \cdot \tag{1}$$

The aethalometer AE33 measured the change of light attenuation through a filter at seven different wavelengths (370 nm–950 nm) and corrected for filter loading effects by two spot sampling to eliminate nonlinearities in light attenuation (Drinovec et al., 2015). A

wavelength-independent scattering correction factor $C = 1.39$ provided by the manufacturer for the build-in filter tape was used. The Ångström absorption exponent *AAE* was calculated from the absorption at all wavelengths. The aethalometer was operated with a total aerosol flow of 2 L/min and an integration time of 1 s for at least 30 s. The PAX combines a wide-angle integrating reciprocal nephelometer to measure scattering and a photoacoustic cell to measure absorption in parallel. In the experiments, a PAX with a wavelength of 870 nm was used to determine the absorption coefficient b_{abs} and the single scattering albedo *SSA* of the generated soot particles at this wavelength. The PAX was calibrated in a two-step process (Arnott, Moosmüller, & Walker, 2000; Nakayama, Suzuki, Kagamitani, & Ikeda, 2015): the scattering channel (reciprocal nephelometer) of the instrument was calibrated against extinction measurements based on Lambert-Beer's law using high concentrations of polydisperse ammonium sulfate aerosol. The photoacoustic channel (absorption cell) was cross calibrated against scattering and extinction measurements based on the relation "absorption = extinction – scattering" by using EC-rich soot particles from the miniCAST 5201 BC generator. The sample flow was 1 L/min and the data averaging time was chosen to be 60 s, with background (zero) measurements being performed for 1 min every 5 min. Mean value and standard deviation of the scattering coefficient b_{scat} and the absorption coefficient b_{abs} were calculated from at least 10 min of measurement. The single scattering albedo *SSA* at $\lambda = 870$ nm was then calculated from the scattering and absorption coefficients according to equation (2). The eBC mass concentration was determined from b_{abs} (870 nm) by using the *MAC* value defined by the manufacturer (4.74 m^2/g at $\lambda = 870$ nm) which is representative of uncoated soot. If not stated otherwise, all eBC mass concentrations given were determined with the PAX.

$$SSA = \frac{b_{scat}}{(b_{scat} + b_{abs})}. \tag{2}$$

For filter sampling, the aerosol was sampled undiluted at a flow rate of 1.2 L/min on two quartz fiber filters placed on top of each other (Advantec, Japan, QR-100, 47 mm, prebaked at 500 °C for 1.5 h). The aerosol had already passed through a denuder filled with activated charcoal and a silica gel diffusion dryer as shown in path b) of Fig. 1. To investigate the composition of the coated soot particles, an OC/EC Analyzer (Lab OC-EC Aerosol Analyzer, Sunset Laboratory Inc., USA) was used, which classified the carbonaceous material as EC and OC. The EUSAAR2-protocol (Cavalli, Viana, Yttri, Genberg, & Putaud, 2010) was modified by extending the last temperature step (850 °C) from 80 s to 120 s in order to ensure complete evolution of carbon. OC, EC and TC (total carbon = sum of OC and EC) masses were calculated based on instrument calibration with sucrose solutions. The OC and TC masses were then corrected by subtracting the OC mass from the gas phase adsorbed on the backup filter (i.e. bottom filter of the two superimposed filters in filter holder) (Mader et al., 2003; Moallemi et al., 2019). The uncertainty of the corrected OC and EC masses was calculated by propagating the uncertainties given by the instrument's software, calculated as the detection limit of 0.2 $\mu gC/cm^2$ plus 5% of the carbon mass determined in the analysis for each carbon fraction. Uncertainties related to the determination of the split point could not be quantified and were therefore not taken into account. Note that in path b) of Fig. 1 no rotating disc diluter was used upstream of the filter holder in order to reduce the sampling time. To test whether the absence of the dilution unit, and consequently the higher concentration of semi-volatile material in the gas phase, can lead to a larger fraction of SOM condensing on the soot particles, EC/TC mass fraction measurements were repeated with and without the dilution unit while keeping all other experimental parameters the same. The analysis showed that the deviation in the EC/TC mass fraction between the two experiments was smaller than or equal to the usual fluctuation of the EC/TC mass fraction observed between two filters sampled with an identical setup. This indicates that the absence of a dilution unit in path b) compared to paths a) and c) does not introduce any measurement artefacts.

To determine the effective density of selected aerosols and to compare electric mobility and aerodynamic diameters, the aerosol was delivered to a DMA (equipped with a ^{85}Kr radioactive source), an Aerosol Particle Mass Analyzer APM (with a ^{85}Kr radioactive source upstream) and an Aerodynamic Aerosol Classifier AAC according to path c) of Fig. 1. The APM, AAC and DMA were validated with PSL (polystyrene) particles of certified size. The mobility size distribution was determined with an SMPS comprising an Electrostatic Classifier (Series 3080, DMA 3081, 3 L/min sheath air, TSI Incorporated, Shoreview, USA) and a CPC (3776 low flow 0.3 L/min, TSI Incorporated, Shoreview, USA) operated with the commercial software (AIM 9.0.0.0, TSI Incorporated, Shoreview, USA, scan 14–980 nm). The aerodynamic particle size distribution was determined by the AAC (Cambustion Limited, Cambridge, UK) (Johnson, Irwin, Symonds, Olfert, & Boies, 2018; Tavakoli & Olfert, 2014) in combination with a CPC (3776 low flow 0.3 L/min, TSI Incorporated, Shoreview, USA) and its commercial software (stepping mode, 50–550 nm, 17 size bins). The APM (APM-II, Model 3601, Kanomax USA, Inc., Andover, USA), operated with an in-house LabVIEW program (scan 0.05–25 fg), was coupled with a CPC (3776 low flow 0.3 L/min, TSI Incorporated, Shoreview, USA).

Note that the APM-CPC measures the mass-to-charge distribution of the aerosol rather than the mass distribution. In this study, we used the particle mass that corresponds to the peak of the measured distribution, assuming a single charge. Multiply charged particles may introduce a bias, however, this interference is expected to only have a small impact given that a ^{85}Kr neutralizer is used upstream of the APM and that the mobility diameter mode always remained in a range in which singly charged particles dominate over multiply charged particles.

By combining the SMPS and APM data, the effective density ρ_{eff} of the particles could be calculated from particle mass and geometric mean mobility diameter according to equation (3) (Gysel, Laborde, Olfert, Subramanian, & Gréhn, 2011; Kulkarni, Baron, Sorensen, & Harper, 2011):

$$\rho_{eff} = \frac{6\,m}{\pi GMD_{mob}^3} \tag{3}$$

The average effective densities reported in this study refer to polydisperse aerosols, and thus reflect both the distribution of

densities at one particle size and the changes in effective density as the size of the soot particles varies within the polydisperse size distribution. This average effective density is approximately comparable to the mean effective density of size-selected particles at the modal diameter (GMD_{mob}) as unimodal size distributions with a small to moderate GSD_{mob} were probed.

3. Results and discussion

3.1. Coating of soot particles with photo-oxidation products of α-pinene

Polydisperse soot particles with specific geometric mean mobility diameters GMD_{mob} were used for the experiments. A setpoint resulting in $GMD_{mob} = 95$ nm was chosen for most experiments, but other sizes were also studied to investigate the influence of the BC core size (see Figures S8, S9 and S10 in the supporting information). Particle size and number concentration were kept constant throughout the day by operating the miniCAST at a fixed operation point. The soot particles were subsequently coated with photo-

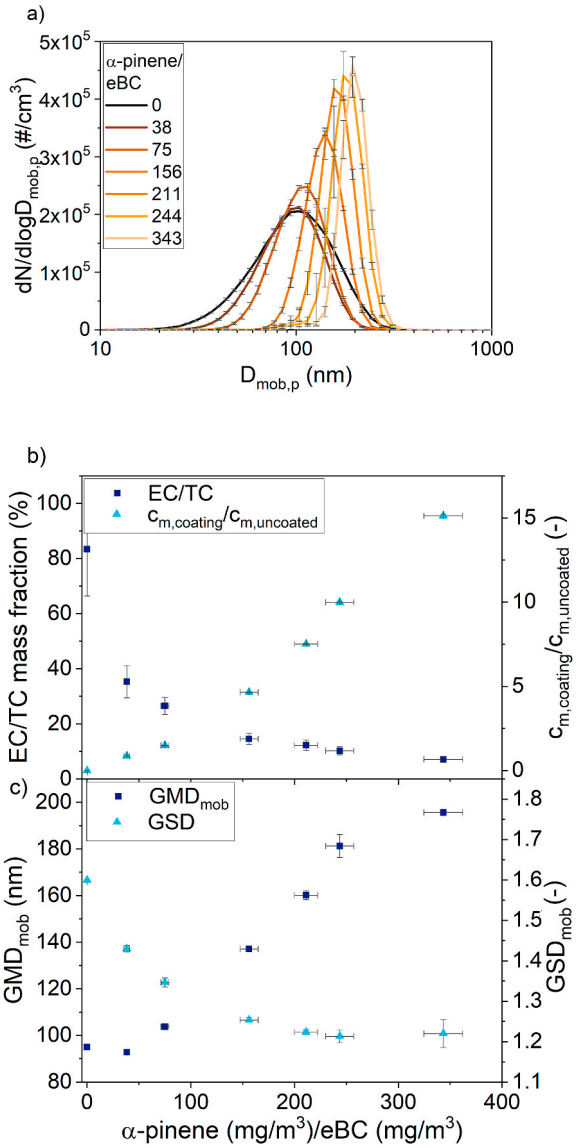

Fig. 2. a) Mobility size distributions of the uncoated (black line) and coated soot particles. The α-pinene to eBC mass ratio is designated in the legend. b) EC/TC (elemental carbon to total carbon) mass fraction and particle mixing state (ratio of SOM coating mass to BC core mass estimated from TEOM mass concentrations) and c) the corresponding geometric mean mobility diameter GMD_{mob} and geometric standard deviation GSD_{mob} of the mobility size distributions as a function of the α-pinene to eBC mass concentration ratio fed into the MSC. The mobility diameter of the uncoated soot particles was kept fixed at 95 nm, and the eBC mass concentration to about 1 mg/m^3. eBC stands for equivalent black carbon. The error bars designate standard deviations (coverage factor $k = 1$; 68% confidence level).

oxidation products of α-pinene (at 5% RH) in a series of experiments as shown in Fig. 2. The eBC mass concentration for the 95 nm soot particle series amounted to 1.1 mg/m^3 (PAX) and the total mass concentration to 1.7 mg/m^3 (TEOM). An EC mass concentration of about 1.3 mg/m^3 was inferred from the total mass measured by the TEOM and the OC/EC mass ratio quantified by the thermo-optical method using the additional assumption that $total\ mass = 1.6 \cdot OC + EC$ (Aggarwal & Kawamura, 2009). This is in reasonable agreement with the aforementioned eBC mass concentration measured by the PAX. It was not possible to precisely determine the EC mass concentration from the thermo-optical analysis due to the different dilution factor in path a) compared to path b) of Fig. 1. The concentration of α-pinene vapors introduced into the MSC was increased in a stepwise manner from 0 mg/m^3 to 400 mg/m^3. SOM from the oxidation of the gas-phase α-pinene condensed on the soot particle surface, shifting GMD_{mob} from 95 nm (black trace in Fig. 2a) to about 195 nm (pale orange trace in Fig. 2a) for the highest precursor gas concentration. Precursor gas and soot seed concentration entering the MSC are relevant for gas-to-particle conversion dynamics (relative humidity which also plays an important role is discussed below), thus VOC to eBC mass ratios in the MSC were used to refer to experiments or compare them. As expected, the higher the ratio of α-pinene vapors to soot mass in the MSC the larger the shift of the size distribution and the larger the GMD_{mob} as more and more material condenses on the soot particles. For this series of experiments, it can be seen, however, that as soon as the ratio of α-pinene to soot mass increased above 150, a second peak appeared in the mobility spectra shown in Fig. 2a. This peak, located at around 110 nm, resulted from the homogeneous nucleation and growth of pure SOM particles due to the high concentration of gas-phase α-pinene in the reactor. Nevertheless, the fraction of nucleation particles remained below 5% in total number concentration and could thus be neglected when interpreting the results of the coating experiments.

At even higher α-pinene to eBC mass ratios in the MSC though, the relative contribution of the nucleation peak can increase quickly, giving rise to a bimodal size distribution. The threshold for this change in gas-to-particles conversion regime primarily depends on the α-pinene to soot mass ratio with homogeneous nucleation occurring at high ratios. The resulting SOM coating thickness also depends on precursor gas to soot mass ratio: A low α-pinene to soot mass ratio in the MSC results in thin SOM coatings even at high α-pinene concentrations (see Fig. S9 of the supporting information). Hence, homogeneous nucleation imposes an upper limit to SOM coating thickness that can be achieved for a given residence time in the MSC. This highlights the importance of carefully adjusting both the mass concentration of the soot seed particles and the ratio of precursor gas to soot mass.

The composition of the particles was determined with thermo-optical analysis and the results are presented as EC/TC mass fraction in Fig. 2b. As soon as α-pinene was mixed with soot, even at a relative low α-pinene to soot mass ratio (m (α-pinene)/m (eBC)≈38), the EC/TC mass fraction decreased steeply from approximately 90% for the uncoated soot to 35%. Surprisingly, the mobility diameter of the coated soot particles did not change (Fig. 2a & c). These observations can be explained with two possible effects: i) the decrease in dynamic shape factor dominates over the increase of volume equivalent diameter and/or ii) restructuring of the soot core during coating condensation as reported in previous smog-chamber and OFR studies with soot particles and different coating materials (Khalizov et al., 2009; Pei et al., 2018; Schnaiter et al., 2005; Weingartner, Burtscher, & Baltensperger, 1997; Weingartner, Baltensperger, & Burtscher, 1995). At EC/TC mass fraction below ≈35%, even a small increase in the SOM mass led to a further decrease in the EC/TC mass fraction (Fig. 2b) and a visible increase in the GMD_{mob} of the particle size distribution. This is in agreement with the findings of Pei at al (Pei et al., 2018), who reported that the major morphological transformation of soot particles coated with limonene oxidation products (and sulfuric acid) occurs sequentially in a stepwise manner and with Wang et al. (Wang et al., 2017) who analyzed the mixing structures and morphology of ambient soot using transmission electron microscopy. First a decrease of shape factor and, possibly, a restructuring of the soot core counteract volume increase effect on mobility diameter for thin coatings. The mobility diameter only starts increasing with increasing coating volume once the particles have reached almost spherical shape, such that no further decrease of shape factor occurs.

The *GSD* (geometric standard deviation, Fig. 2c of the mobility size distribution became narrower and thus more uniform as more SOM was added to the (growing) particles. Similar changes have also been observed in a smog-chamber experiment, where the median mobility diameter of the particles more than doubled, while the *GSD* of the size distribution decreased by a remarkable 30% (Schnaiter et al., 2005). Two effects contribute to the narrowing of the *GSD*: i) condensation generally leads to a decrease in GSD_{mob} as GMD_{mob} increases due to condensation growth and ii) collapsing of the soot particles, if particles with above and below average fractal-like dimension are enriched below and above the peak mobility diameter, respectively, such that the shape factor change has a smaller or greater effect on particle mobility.

The variation of α-pinene in the MSC within the range accessible without triggering homogeneous nucleation allows to continuously increase GMD_{mob} by up to a factor of 2, e.g. from initially 100 nm to about 200 nm, as shown in Fig. 2c. For the same particle size, Pei et al. (Pei et al., 2018), who enhanced SOM condensation on monodisperse soot by pre-activating the soot surface with a sulfuric acid coating, reported a slightly lower maximum mobility diameter increase of 1.6. For other soot particle sizes the authors reported factors ranging from 1.1 (for 200 nm soot cores) to > 2.1 (for 75 nm soot cores) (Pei et al., 2018).

The mixing state of (aged) atmospheric BC particles is often reported in terms of the mass ratio of coating to BC core. For example, Yuan et al. (Yuan et al., 2020) reported coating-to-core mass ratios of 1 to 4 for aerosol observations at a rural site in Germany during the winter season, and Cappa et al. (Cappa et al., 2019) observed coating-to-core ratios of 1 to 13 for two Californian cities. In the herein presented study, the BC particle mixing state was quantified from mass concentrations measured by the TEOM. The mixing state presented as coating to core mass ratio in Fig. 2b was calculated as $C_{m,coating}/C_{m,uncoated} = (C_{m,coated} - C_{m,uncoated})/C_{m,uncoated}$, thereby assuming a constant output of the miniCAST. $C_{m,coated}$ and $C_{m,uncoated}$ are the mass concentrations of coated and uncoated soot particles, respectively. The particles with the thinnest coating, generated at an α-pinene-to-soot mass ratio in the MSC of 38 (35% EC/TC and $GMD_{mob} = 93$ nm), exhibited a coating-to-soot core mass concentration ratio close to 1. Particles with the thickest coating, generated at an α-pinene-to-soot mass ratio in the MSC of 343 (7% EC/TC and $GMD_{mob} = 196$ nm), possessed a coating-to-soot core mass

concentration ratio of 15. Thus, the particle mixing states attainable with the combination of miniCAST and MSC cover the full range reported in the literature for atmospheric BC particles.

The change of morphological properties upon coating of the soot particles with SOM can be further supported by comparing the evolution of the geometric mean mobility and aerodynamic diameters. Fig. 3a shows the geometric mean mobility diameter GMD_{mob} and the mean aerodynamic diameter of uncoated and coated soot particles as a function of their mass. For uncoated soot particles (particle mass 0.44 fg), GMD_{mob} (112 nm) was larger than the geometric mean aerodynamic diameter GMD_{aero} (75 nm) as the effect of the high dynamic shape factor of loose aggregates dominates over the material density effect (DeCarlo, Slowik, Worsnop, Davidovits, & Jimenez, 2004).

After the first coating step, the particle mass increased to around 1.35 fg, and the relation between the geometric mean mobility and geometric mean aerodynamic diameters changed drastically. As discussed before, adding SOM to the irregular fractal soot particles can lead to a decrease of the dynamic shape factor and, possibly, a restructuring of the soot core. With the mobility diameter being proportional to the dynamic shape factor, the decrease of the latter as the particles become more compact counteracts the increase in volume equivalent diameter by the condensed SOM and the GMD_{mob} remained almost unchanged. In contrast, the aerodynamic diameter (in the limit of the continuum regime) is proportional to the square root of particle density and inversely proportional to the square root of the dynamic shape factor. Thus, the decrease of the dynamic shape factor along with the increase in particle volume diameter upon addition of SOM both contribute to an increase in the aerodynamic diameter. As a result, after the first coating step the aerodynamic diameter almost tripled compared to that of the uncoated soot, thus exceeding the mobility diameter. By adding further SOM, both the mobility and the aerodynamic diameter increased only slightly as no drastic change in dynamic shape factor or particle density occurred. The relation between mobility and aerodynamic diameter for the coated particles was linear with a slope of 0.7 (see Fig. S3).

The assumption that the morphological transformation of soot particles upon coating occurs sequentially in a stepwise manner, with filling of void space and soot particle collapse first and growth of the mobility diameter in a second stage, can also be supported when investigating the average effective density of the particles as a function of mobility diameter (Fig. 3b). Upon SOM condensation, the average effective density increased from 0.58 g/cm^3 all the way up to about 1.2 g/cm^3 with very small concurrent increase of the mobility diameter from 112 nm to 129 nm. The average effective density with coating matches approximately the expected material density of the particle, thus indicating near-spherical particle shape. Further condensation of SOM resulted in increasing mobility diameter, while the average effective density remained almost constant, both of which can be explained by the fact that the particle shape did not change any further. The average effective densities displayed in Fig. 3b agree satisfactorily with the effective densities of ≈1.2–1.5 g/cm^3 reported for size-selected aged soot particles in a near-traffic urban environment (Rissler et al., 2014).) In particular, when the content of salts, such as ammonium nitrate and ammonium sulfate, was low and the organic content of the particles high, the effective density of the aged soot particles dropped to ~1.3 g/cm^3, which agrees very well with the value of 1.2 g/cm^3 reported in our study. As already noted in section 2.2, the average effective densities reported in our study refer to polydisperse aerosols, and thus reflect both the distribution of densities at one particle size and the changes in effective density as the size of the soot particles varies within the polydisperse size distribution. This average effective density is approximately comparable to the mean effective density of size-selected particles at the modal diameter (GMD_{mob}) as unimodal size distributions with a small to moderate GSD_{mob} were probed.

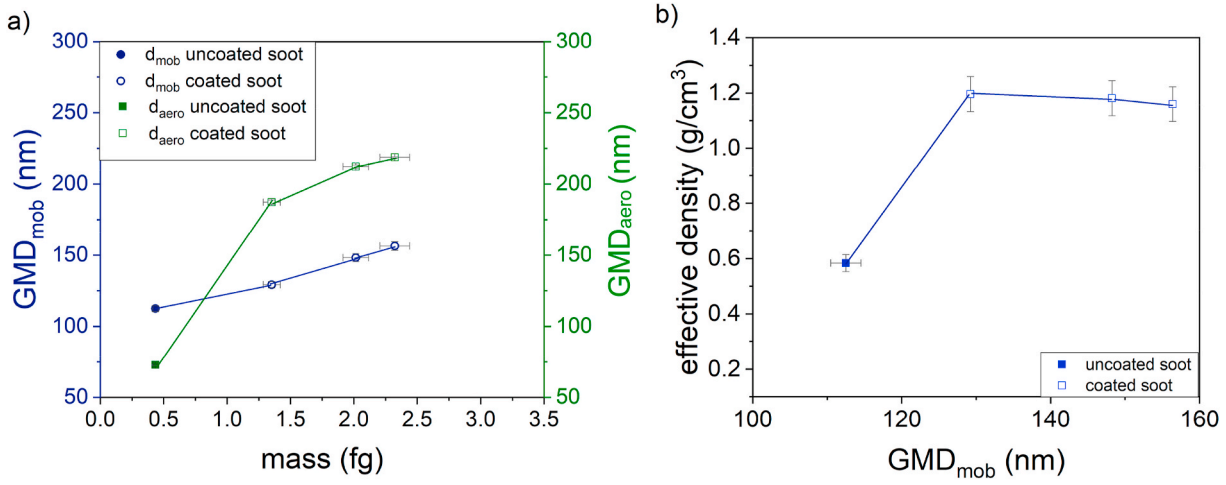

Fig. 3. a) Geometric mean mobility diameter (GMD_{mob}) and geometric mean aerodynamic diameter (GMD_{aero}) as a function of the particle mass (i.e. the mass relative to the peak of the mass distribution as resulting from the APM scans. b) average effective density of uncoated soot particles (filled symbols) and the same soot particles coated with SOM (hollow symbols) dependent on GMD_{mob} of the polydisperse sample (see main text). The error bars designate standard deviations (coverage factor $k = 1$; 68% confidence level).

3.2. Optical properties of coated soot particles

Concerning the optical properties of the coated soot, the aerosol absorption Ångström exponent, *AAE,* was used as measure for the wavelength dependence of the absorption and the single scattering albedo, *SSA* at 870 nm, as a measure for the strength of scattering with respect to light extinction. Fig. 4 shows that the *SSA* increased almost linearly from about 0.02 for the uncoated soot particles to about 0.7 for highly coated soot particles. This is primarily the result of condensing weakly light-absorbing SOM on strongly light-absorbing BC cores, whereas size dependence of mass scattering efficiency also comes into play. This is in agreement with the smog-chamber study by Schnaiter et al. (Schnaiter et al., 2005) where diesel soot was coated with α-pinene SOM. In their study, the soot particles also underwent a transition with increasing number of coating steps from light-absorbing BC-like material (with SSA at 700 nm of about 0.13) to coated spheres, in which the soot cores were fully embedded in the SOM matrix and thus scattering dominated absorption (*SSA* at 700 nm of about 0.75). The main difference is the timescale of the two experiments; in the smog-chamber the soot particles were coated stepwise within hours, while the coating in the MSC provides a continuous stable aerosol sample at high concentration and flow rate, and its properties can be varied over a wide range within seconds.

Moreover, the SSA values displayed in Fig. 4 simulate satisfactorily the SSA range of aged soot particles in ambient air. For instance, in Mexico City (Mexico), it was observed that the aged soot particles had a count median diameter of 160 nm and SSA of 0.64 while the aged soot particles at Riverside (California, USA) had a count median diameter of 210 nm and SSA of 0.81 (Moffet & Prather, 2009). It must be noted, however, that the aged soot particles investigated by Moffet et al. were internally mixed with both SOM and inorganic species, which prevents a direct comparison with our study.

The aerosol *AAE* increased from 1.3 for the uncoated soot to 1.5 already after the first coating step as shown in Fig. 4, indicating that even a relatively low coating to core mass ratio of 0.9 can have a considerable effect on the spectral dependence of light absorption. This increased *AAE* can be attributed to the strong wavelength dependence of the SOM, in agreement with Lambe et al. (Lambe et al., 2013) who reported a high *AAE* of >7 for pure α-pinene SOA in the wavelength range 300–500 nm, combined with sufficient MAC such that the SOM absorption becomes relevant compared to absorption by BC. By increasing the α-pinene to eBC mass ratio further (see Fig. 4), the *AAE* increased only slowly and reached a plateau value of ≈1.65 at a ratio of coating mass to soot core mass of the coated particles of about 7.5 (α-pinene to soot mass ratio in the MSC of about 200). The range of *AAE* attained in our study (approx. 1.3–1.7) is realistic and compares well with the findings of field studies. According to Zhang et al. theoretical calculations and field studies have shown that the range of AAE for internally mixed BC particles varies approximately in the range from 1 to 1.7, depending on the size and optical properties of the particle core and non-absorbing coating and the wavelength pairs used to determine AAE (see Zhang et al., 2018, and references therein).

Further experiments with different soot core sizes and mass concentrations are reported in Figure S 9 (polydisperse particles with GMD_{mob} 160 nm) and Figure S 10 (polydisperse particles with GMD_{mob} 34 nm) in the Supporting Information.

To summarize, even though the α-pinene to eBC mass concentration ratios in the MSC are in the range from 40 to 400 and thus considerably higher than what is encountered in ambient air, the physico-chemical properties of the coated soot particles (EC/TC mass fraction, mobility diameter, effective density, SSA and AAE) are realistic as shown in sections 3.1 and 3.2.

3.3. Conversion efficiency of alpha-pinene to SOM in the MSC

The MSC conversion efficiency *CE* (not to be confused with "yield") was calculated according to equation (5). $C_{m,\ coated}$ and $C_{m,uncoated}$ are the mass concentrations of the uncoated and coated soot aerosols, respectively, measured with the TEOM and $C_{m,\alpha-pinene}$ the mass concentration of α-pinene in the MSC. A MSC conversion efficiency between 3.5 and 6% was determined for $C_{m,\alpha-pinene}$ in the range 40–400 mg/m^3, with the mass concentration of soot seed particles kept constant at ≈1 mg/m^3 and at RH ≤ 5%.

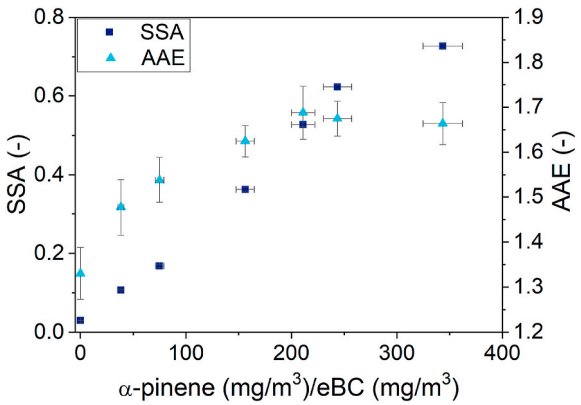

Fig. 4. *SSA* (left axis) and *AAE* (right axis) as a function of the α-pinene to eBC mass concentration ratio fed into the MSC. The mobility diameter of the uncoated soot particles was set to 95 nm. SSA and AAE stand for single scattering albedo and absorption Ångström exponent, respectively. eBC stands for equivalent black carbon. The error bars designate standard deviations (coverage factor $k = 1$; 68% confidence level).

$$CE = \frac{C_{m,coated} - C_{m,uncoated}}{C_{m,\alpha-pinene}}. \quad (5)$$

The number of lamps switched on in the MSC and thus the ozone concentration had hardly any effect on the conversion efficiency and thus the size of the particles. In the absence of ozone (all UVC lamps switched off) no SOM formation took place (with an α-pinene concentration of about 100 mg/m^3 and an eBC mass concentration of 1 mg/m^3) and no change in the properties of the soot particles was observed, as expected. When one lamp was switched on (≈30 mg/m^3 ozone), coating of soot particles with SOM led to a narrowing of the mobility size distribution and a shift of the GMD_{mob} towards larger values. Switching on additional UVC lamps (≈30 mg/m^3 ozone per lamp, leading to 60–120 mg/m^3 ozone in total) enhanced the SOM formation only slightly compared to the experiments with one lamp, and had a negligible effect on the particle size distributions and optical properties of the aerosols (see Fig. S4 in the supporting information). This series of experiments indicate that despite the high concentration of α-pinene, no α-pinene condensed on the particles without prior oxidation by ozone. Only the oxidation products of α-pinene condensed on the soot particles due to the fact that oxidation decreases the volatility of VOCs by adding functionalities to the molecules and by dimerization (Donahue, Kroll, Pandis, & Robinson, 2012; Zhang et al., 2015).

By humidifying the aerosol to 75% RH, the conversion efficiency of α-pinene to SOM increased strongly. For instance, with an α-pinene gas-phase concentration of 90 mg/m^3 and an eBC mass concentration of 1.3 mg/m^3 under dry conditions (5% RH) the GMD_{mob} of the (uncoated) soot particles increased by a factor of 1.3. Upon humidification to 75% RH, GMD_{mob} readily increased by a factor of 2.2 compared to the uncoated soot. The conversion efficiency of α-pinene was so high in this case that the available condensation sink offered by the soot particles was insufficient to prevent homogeneous nucleation. Additionally to the coating of the soot particles, SOM particles with a GMD_{mob} of about 100 nm were generated by homogenous nucleation (see Fig. S5 in the supporting information). This highlights the importance of humidity control during the experiments in order to increase the particle growth but at the same time suppress particles due to homogeneous nucleation of the gas-phase VOCs. By careful adjustment of the relative humidity, the experimental conditions can be optimized to achieve a maximum growth of soot particles with minimum nucleation of SOM. To enhance aerosol stability and reproducibility while keeping the design of the setup as simple as possible, low RH in a readily controlled manner is favorable, and the different particle properties should be tuned by primarily varying the α-pinene concentration and

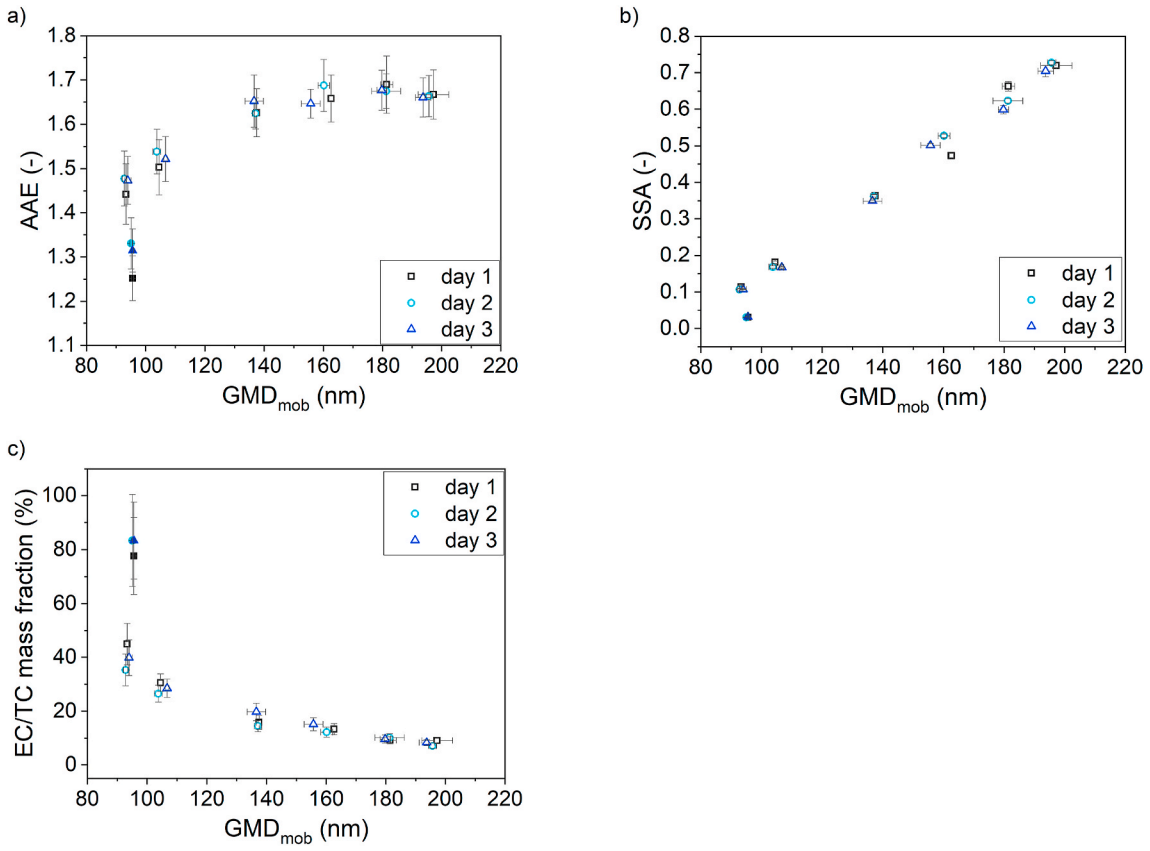

Fig. 5. A) *AAE* (absorption Ångström exponent), b) *SSA* (single scattering albedo) and c) EC/TC (elemental carbon to total carbon) mass fraction of the uncoated (95 nm, filled symbols) and coated (hollow symbols) soot particles as a function of the geometric mean mobility diameter GMD_{mob} at three different days. The error bars in a) and b) designate experimental standard deviations (k = 1; 68% confidence level). The error bars in c) designate the uncertainty in the determination of the EC/TC mass fraction.

secondarily the ozone concentration. It must also be noted that different humidity as well as different ozone or α-pinene concentrations can affect the chemical composition of the oxidation products. The exact molecular composition of the SOM is not relevant when calibrating soot photometers but can be important when performing health related studies with model aerosols.

3.4. Stability and reproducibility of the coating of soot particles

The stability of the generated aerosol was monitored for about 2 h by measuring the mobility size distribution and the aerosol mass concentration of the uncoated and coated soot particles. The results regarding particle size can be found in the supporting information (Fig. S12). The mobility diameter and particle number concentration of the uncoated soot particles remained stable in time with a standard deviation within 1% and 6%, respectively. The mass concentration was also stable, with a reduced $R^2 > 0.99$ for the fit between total mass and measurement time.

However, for the coated soot particles a slow increase in the GMD_{mob} was observed with time, with a standard deviation of 1–2% during 2 h of measurement. This was due to a drift in the concentration of α-pinene entering the MSC. As mentioned in section 2.1, the concentration of gas-phase α-pinene was controlled by adjusting the flow of zero-air through the VOC container with a MFC. Since the zero-air flow remained stable, the gradual increase in the amount of α-pinene reaching the MSC was probably due to physical processes (e.g. saturation of adsorption sites at the surface) in the VOC container and aerosol tubes. This drift in the α-pinene mass concentration could be remedied by slightly decreasing the zero-air flow through the α-pinene container with time. This helped to keep the variability (relative standard deviation) in size (GMD_{mob}) and total particle number concentration within 2% and 6%, respectively.

To assess the reproducibility of the aerosol generation, a series of coating experiments was performed at three different days. The experimental results in terms of measured GMD_{mob}, *AAE*, *SSA* and EC/TC mass fraction are shown in Fig. 5. The parameters are plotted as a function of GMD_{mob}. Despite day-to-day variations in the total number concentration of the soot particles (up to 10% (Ess & Vasilatou, 2019)) or in the concentration of the gas-phase SOM precursor, the same α-pinene/eBC mass ratios in the MSC could be reproduced every day by adjusting the flow of zero-air through the VOC bottle. Small adjustments of typically 1–10 mL/min sufficed. Similar GMD_{mob} could be achieved on different days, with inter-day standard deviations smaller than 2% at each α-pinene/eBC mass concentration ratio. The *AAE* measurements shown in Fig. 5a) exhibit, however, a larger day-to-day variability even in the case of uncoated soot. Still, the standard deviations between measurements performed on different days lie well within the statistical uncertainties and are smaller than 3%. The *SSA* as a function of GMD_{mob} (see Fig. 5b) is quite similar on different days with standard deviations of less than 6%. As visible in Fig. 5c), the EC/TC mass fractions show a higher variability with standard deviation up to 16%. Besides true variations in the particle composition, the overall higher uncertainty of the EC/OC analysis might also be a reason for this variation. To conclude, by combining a miniCAST 5201 soot generator with a MSC it was possible to coat soot particles with SOM from the oxidation of α-pinene in a stable and reproducible manner.

3.5. Coating of soot particles with photo oxidation products of mesitylene

In previous studies, the formation of SOM from mesitylene (Fick, Pommer, Nilsson, & Andersson, 2003; A. T.; Lambe, Onasch, et al., 2011; Molteni et al., 2018, pp. 1909–1921; Vivanco et al., 2011; Wyche et al., 2009) has not been investigated as extensively as the SOM formation from α-pinene (Berndt, Böge, & Stratmann, 2003; Fick et al., 2003; Pospisilova et al., 2020; Saathoff et al., 2003b; Schnaiter et al., 2005; Tillmann et al., 2010), even though mesitylene can serve as surrogate for anthropogenic VOCs. Ozonolysis of certain SOM precursors is known to be inefficient, but oxidation can be promoted by OH radicals (Tillmann et al., 2010; Zhou et al., 2011). As ozonolysis of mesitylene at dry conditions is very inefficient (see supporting information Figure S 6), the aerosol needed to be humidified (37–40% RH) to induce generation of OH radicals. The evolution of the 95 nm GMD_{mob} soot core particles upon coating with increasing amounts of mesitylene SOM, analog to the coating with SOM from α-pinene in the previous sections, can be found in the supporting information (Figure S 7a) together with a plot of the GMD_{mob} and EC/TC mass fractions as a function of the mesitylene to eBC mass ratio (Figure S 7 b). By adding low amounts of gas-phase mesitylene in the MSC, the mobility size distribution shifted to smaller diameters while the distribution became narrower. As discussed for the α-pinene experiment, this indicates a decrease of the shape factor and a possible restructuring of the soot core. The decrease in the shape factor counteracts the increase in mobility diameter due to condensation of SOM on the soot surface. From there on, increasing the concentration of gas-phase mesitylene led to an increase of the GMD_{mob} as further SOM condenses on the particles. Similar observations were made when using α-pinene as SOM precursor (see Subsection 3.1). It can thus be concluded that SOM interacts with the soot particles in similar ways regardless of its formation mechanism (i.e. primarily ozonolysis of α-pinene versus OH oxidation of mesitylene). This can also be supported by the fact that *SSA*, *AAE* and EC/TC mass fraction of the soot particles coated with α-pinene or mesitylene SOM were similar for comparable particle sizes, if identical soot particles are used as seed particles (see Fig. S8). It also implies that the physico-chemical properties of SOM from these two precursor gases are sufficiently similar to cause very limited differences in resulting optical properties of soot particles with equal coating volume and core size.

GMD_{mob} could be increased by almost a factor of 2 with mesitylene (Fig. 6), as with α-pinene. In the case of mesitylene, however, a lower VOC concentration was needed than in the case of α-pinene due to additional oxidation by OH radicals. Nevertheless, longer stabilization times of 1 to 2 h were necessary at the beginning of each experiment or when changing the mesitylene gas phase concentration. The reason was the formation of an additional peak due to homogeneous nucleation of SOM particles. With time, this peak decreased without ever vanishing completely, except for very low mesitylene concentrations. Moreover, the mass concentration of gas-phase mesitylene exhibited a more pronounced drift over time and necessitated a larger adjustment (decrease) of the zero air flow by up to 30 mL/min to achieve stable mesitylene mass concentrations during each experiment. This may be due to the much lower vapor

pressure of mesitylene and the longer time needed to achieve steady-state conditions in the VOC container. Adsorption of mesitylene vapors on the surface of the connecting tubes might have also played a role.

As mentioned above, to coat soot with SOM from the oxidation of mesitylene, humidification of the aerosol is necessary (Figure S 6 in the supporting information). When mixing 90 mg/m^3 of gas-phase mesitylene with 0.75 mg/m^3 eBC without humidification (RH<5%), no coating of soot was observed. By increasing RH to 70%, an increase in GMD_{mob} by a factor of 1.7 compared to the uncoated particles was achieved and the MSC conversion efficiency for mesitylene increased to 5–10%.

As shown in Fig. 6 (see corresponding size distributions in Figure S 7a in the supporting information), it was possible to tune the EC/TC mass fraction within a large range (20%–90%) but compared to the experiments with α-pinene SOM the day-to-day variability was much higher. It was challenging to generate the exact mesitylene to eBC mass ratios in the MSC on different days and, even if that happened, the particle properties still differed from day to day. In Fig. 6, the *AAE*, *SSA* and EC/TC mass fraction of the generated aerosols are plotted as a function of the GMD_{mob} on three different days. By comparing the properties of particles with similar GMD_{mob} after coating, the inter-day standard deviation in *AAE*, *SSA* and EC/TC mass fraction was found to be about 3%, 10% and 15%, respectively. We hypothesized that one reason for the lower reproducibility might be the formation of the nucleation mode of mesitylene SOM, which depends strongly on the gas-phase mesitylene concentration and aerosol relative humidity (temperature was approximately constant). Even a careful control of the humidity (40 ± 2% RH) could not reduce the day-to-day variability, despite the fact that a lower humidity, in general, led to a lower concentration of homogeneously nucleated SOM particles.

To conclude, it is possible to coat soot particles with oxidation products of mesitylene, even though this requires greater experimental effort and is subject to higher measurement uncertainties than coating with α-pinene SOM. In general, the results prove that the current experimental setup is versatile and can be used for coating soot particles with SOM from the oxidation of anthropogenic precursors, which often requires generation of OH radicals at high (≈40%) RH. This opens up the possibility for further studies in the future involving other biogenic or anthropogenic precursors or even mixtures of both.

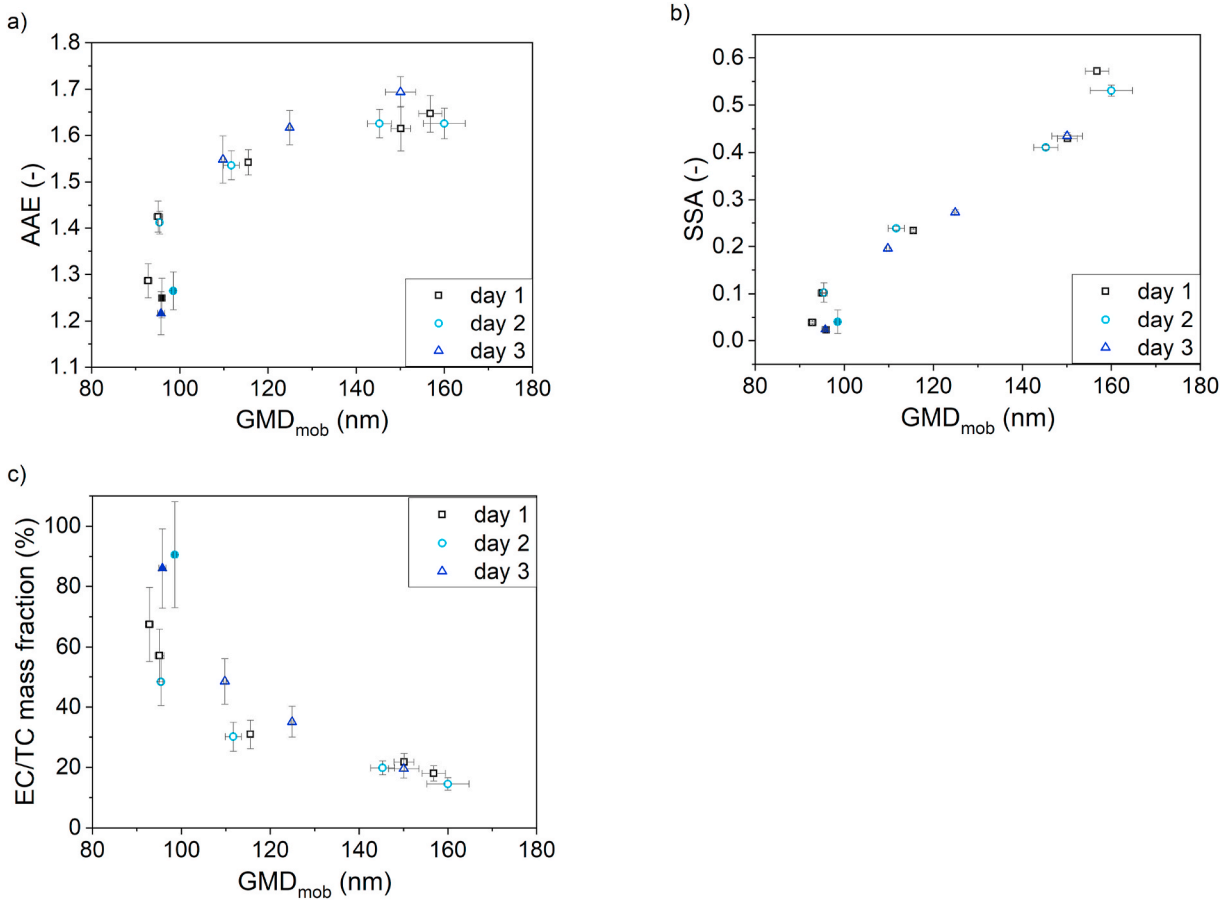

Fig. 6. A) *AAE* (absorption Ångström exponent), b) SSA (single scattering albedo) and c) EC/TC (elemental carbon to total carbon) mass fraction of the uncoated (95 nm, filled symbols) and coated (hollow symbols) soot particles as a function of the geometric mean mobility diameter GMD_{mob} at four different days. The soot mass concentration was about 0.6–0.9 mg/m^3 (PAX) and the mesitylene concentration ranged from 0 to 280 mg/m^3. For all experiments the humidity was set to 37–40% RH. The error bars in a) and b) designate experimental standard deviations (k = 1; 68% confidence level).

4. Summary and conclusions

In this study, a simple and robust setup for the generation of test aerosols which simulate the optical properties of ambient carbonaceous particles is presented. Soot particles from a miniCAST generator were successfully coated with secondary organic matter, SOM, generated in a Micro Smog Chamber (MSC). α-pinene and mesitylene were used as surrogates for biogenic and anthropogenic volatile organic compounds (VOCs). By adjusting the concentration of the gas-phase SOM-precursor, a series of model aerosols with controlled physical and optical properties were produced, simulating a wide range of atmospherically relevant aerosols.

The model aerosols were characterized with respect to mobility size distribution, single scattering albedo, absorption Ångström exponent and EC/TC mass fraction. Polydisperse soot particles with different sizes (geometric mean mobility diameters of 30 nm, 90–95 nm or 160 nm) were used as seed particles. When coating the soot particles, the α-pinene-to-soot mass concentration ratio in the MSC was carefully optimized for each soot core size separately, since this was the main factor determining the properties of the generated particles. The uncoated soot cores had very low single scattering albedo ($SSA_{870nm} \leq 0.1$), an absorption Ångström exponent close to 1 (AAE <1.3) and high EC/TC mass fractions (>80%). Coating with gradually increasing amounts of SOM led to particle growth by a factor of up to 2 in mobility diameter and a simultaneous transformation into highly scattering particles (SSA_{870nm} up to 0.7), with increased absorption Ångström exponents ($AAE \approx 1.7$) and high organic carbon content (EC/TC mass fraction < 10%). When using α-pinene as SOM-precursor under dry conditions (5% RH), high stability over several hours could be achieved, with a standard deviation in particle size and number concentration of ≤1% and ≤6%, respectively. The day-to-day reproducibility was also satisfactory, with a standard deviation in particle size, optical properties (SSA and AAE) and EC/TC mass fraction smaller than 2%, 6% and 16%, respectively.

When using mesitylene as SOM-precursor, a higher level of humidity was necessary for SOM formation in the MSC. Thus, a compromise had to be found with high enough humidity to enable oxidation of mesitylene through formation of OH radicals but at the same time low enough to avoid formation of homogeneously nucleated SOM particles. In general, the experiments with mesitylene proved to be quite challenging and the day-to-day reproducibility was not as satisfactory as in the case of α-pinene.

Compared to large smog chambers, the combination of a miniCAST generator with a MSC offers advantages, such as short reaction times in the order of a few seconds, high flexibility in tuning the particle properties, compactness and standardization potential. Compared to other oxidation flow reactors reported in the literature, the use of the MSC enables generation of aerosols at high number (10^6 #/cm^3) and mass concentrations (up to 15 mg/m^3, depending on particle size and SOM mass fraction), a prerequisite for challenging several absorption photometers (or other aerosol instruments) in parallel.

The carbonaceous aerosols generated in this study can find useful applications in the field of aerosol instrument calibration, particularly in the standardization of filter-based absorption photometers in the laboratory under controlled conditions. Other possible applications include health-related studies and laboratory-based filter testing (e.g. filter retention efficiency and aging properties). Future work will focus on miniaturizing and further standardizing the aerosol generation setup with the aim to develop a transfer standard suitable for in-field operation.

Declaration of competing interest

The authors declare that they have no known competing financial interests or personal relationships that could have appeared to influence the work reported in this paper.

Acknowledgement and funding

This work was carried out in the context of the EMPIR projects 16ENV07 Aeromet and 18HLT02 AeroTox. EMPIR is jointly funded by the EMPIR participating countries within EURAMET and the European Union. METAS received funding from the 18HLT02 AeroTox project and the Swiss State Secretariat for Education, Research and Innovation (SERI) under contract number 17.00112. KV and AK acknowledge support from the Swiss Federal Office for the Environment through Project 17.0094. PJ. The measurements displayed in Fig. 3 were carried out in the context of the EMPIR 16ENV02 Black Carbon project. PSI was supported by the Swiss State Secretariat for Education, Research and Innovation (SERI) under contract number 17.00117. The opinions expressed and arguments employed herein do not necessarily reflect the official views of the Swiss Government.

Appendix A. Supplementary data

Supplementary data to this article can be found online at https://doi.org/10.1016/j.jaerosci.2021.105820.

References

Aggarwal, S. G., & Kawamura, K. (2009). Carbonaceous and inorganic composition in long-range transported aerosols over northern Japan: Implication for aging of water-soluble organic fraction. *Atmospheric Environment, 43*(16), 2532–2540. https://doi.org/10.1016/j.atmosenv.2009.02.032

Ahlberg, E., Falk, J., Eriksson, A., Holst, T., Brune, W. H., Kristensson, A., et al. (2017). Secondary organic aerosol from VOC mixtures in an oxidation flow reactor. *Atmospheric Environment, 161*, 210–220. https://doi.org/10.1016/j.atmosenv.2017.05.005

Arnott, W. P., Moosmüller, H., & Walker, J. W. (2000). Nitrogen dioxide and kerosene-flame soot calibration of photoacoustic instruments for measurement of light absorption by aerosols. *Review of Scientific Instruments, 71*(12), 4545–4552. https://doi.org/10.1063/1.1322585

Baltensperger, U., Kalberer, M., Dommen, J., Paulsen, D., Alfarra, M. R., Coe, H., et al. (2005). Secondary organic aerosols from anthropogenic and biogenic precursors. *Faraday Discussions, 130*, 265–278. https://doi.org/10.1039/b417367h

Bambha, R. P., Dansson, M. E., Schrader, P. E., & Michelsen, H. A. (2013). Effects of volatile coatings on the laser-induced incandescence of soot. *Applied Physics B, 112*, 343–358. https://doi.org/10.1007/s00340-013-5463-9

Berndt, T., Böge, O., & Stratmann, F. (2003). Gas-phase ozonolysis of α-pinene: Gaseous products and particle formation. *Atmospheric Environment, 37*(28), 3933–3945. https://doi.org/10.1016/S1352-2310(03)00501-6

Bond, T. C., Doherty, S. J., Fahey, D. W., Forster, P. M., Berntsen, T., Deangelo, B. J., et al. (2013). Bounding the role of black carbon in the climate system: A scientific assessment. *Journal of Geophysical Research Atmospheres, 118*(11), 5380–5552. https://doi.org/10.1002/jgrd.50171

Bruns, E. A., El Haddad, I., Keller, A., Klein, F., Kumar, N. K., Pieber, S. M., et al. (2015). Inter-comparison of laboratory smog chamber and flow reactor systems on organic aerosol yield and composition. *Atmospheric Measurement Techniques, 8*(6), 2315–2332. https://doi.org/10.5194/amt-8-2315-2015

Burtscher, H., Schmidt-Ott, A., & Siegmann, H. C. (1988). Monitoring particulate emissions from combustions by photoemission. *Aerosol Science and Technology, 8*(2), 125–132. https://doi.org/10.1080/02786828808959177

Buseck, P. R., Adachi, K., Gelencsér, A., Tompa, É., & Pósfai, M. (2012). Are black carbon and soot the same? *Atmospheric Chemistry and Physics Discussions, 12*, 24821–24846. https://doi.org/10.5194/acpd-12-24821-2012

Cappa, C. D., Lack, D. A., Burkholder, J. B., & Ravishankara, A. R. (2008). Bias in filter-based aerosol light absorption measurements due to organic aerosol loading: Evidence from laboratory measurements. *Aerosol Science and Technology, 42*(12), 1022–1032. https://doi.org/10.1080/02786820802389285

Cappa, C. D., Onasch, T. B., Massoli, P., Worsnop, D. R., Bates, T. S., Cross, E. S., et al. (2012). Radiative absorption enhancements due to the mixing state of atmospheric black carbon. *Science, 337*(6098), 1078–1081. https://doi.org/10.1126/science.1223447

Cappa, C. D., Zhang, X., Russell, L. M., Collier, S., Lee, A. K. Y. Y., Chen, C.-L. L., et al. (2019). Light absorption by ambient black and brown carbon and its dependence on black carbon coating state for two California, USA cities in winter and summer. *Journal of Geophysical Research: Atmosphere, 124*(3), 1550–1577. https://doi.org/10.1029/2018JD029501

Cavalli, F., Viana, M., Yttri, K. E., Genberg, J., & Putaud, J. P. (2010). Toward a standardised thermal-optical protocol for measuring atmospheric organic and elemental carbon: The EUSAAR protocol. *Atmospheric Measurement Techniques, 3*(1), 79–89. https://doi.org/10.5194/amt-3-79-2010

Collaud Coen, M., Weingartner, E., Apituley, A., Ceburnis, D., Fierz-Schmidhauser, R., Flentje, H., et al. (2010). Minimizing light absorption measurement artifacts of the aethalometer: Evaluation of five correction algorithms. *Atmospheric Measurement Techniques, 3*(2), 457–474. https://doi.org/10.5194/amt-3-457-2010

Corbin, J. C., Czech, H., Massabò, D., de Mongeot, F. B., Jakobi, G., Liu, F., et al. (2019). Infrared-absorbing carbonaceous tar can dominate light absorption by marine-engine exhaust. *Npj Climate and Atmospheric Science, 2*(1), 1–12. https://doi.org/10.1038/s41612-019-0069-5

Corbin, J. C., Keller, A., Lohmann, U., Burtscher, H., Sierau, B., & Mensah, A. A. (2015). Organic emissions from a wood stove and a pellet stove before and after simulated atmospheric aging. *Aerosol Science and Technology, 49*(11), 1037–1050. https://doi.org/10.1080/02786826.2015.1079586

Corbin, J. C., Lohmann, U., Sierau, B., Keller, A., Burtscher, H., & Mensah, A. A. (2015). Black carbon surface oxidation and organic composition of beech-wood soot aerosols. *Atmospheric Chemistry and Physics, 15*(20), 11885–11907. https://doi.org/10.5194/acp-15-11885-2015

Corbin, J. C., Moallemi, A., Liu, F., Gagné, S., Olfert, J. S., Smallwood, G. J., et al. (2020). Closure between particulate matter concentrations measured ex situ by thermal–optical analysis and in situ by the CPMA–electrometer reference mass system. *Aerosol Science and Technology, 6826*, 1–17. https://doi.org/10.1080/02786826.2020.1788710

DeCarlo, P. F., Slowik, J. G., Worsnop, D. R., Davidovits, P., & Jimenez, J. L. (2004). Particle morphology and density characterization by combined mobility and aerodynamic diameter measurements. Part 1: Theory. *Aerosol Science and Technology, 38*(12), 1185–1205. https://doi.org/10.1080/027868290903907

Donahue, N. M., Kroll, J. H., Pandis, S. N., & Robinson, A. L. (2012). A two-dimensional volatility basis set – Part 2 : Diagnostics of organic-aerosol evolution. *Atmospheric Chemistry and Physics, 12*, 615–634. https://doi.org/10.5194/acp-12-615-2012

Drinovec, L., Močnik, G., Zotter, P., Prévôt, A. S. H., Ruckstuhl, C., Coz, E., et al. (2015). The "dual-spot" aethalometer: An improved measurement of aerosol black carbon with real-time loading compensation. *Atmospheric Measurement Techniques, 8*(5), 1965–1979. https://doi.org/10.5194/amt-8-1965-2015

Ess, M. N., Bertò, M., Irwin, M., Modini, R. L., Gysel-beer, M., & Vasilatou, K. (2021). *Optical and morphological properties of soot particles generated by the miniCAST 5201 BC generator*. https://doi.org/10.1080/02786826.2021.1901847

Ess, M. N., & Vasilatou, K. (2019). Characterization of a new MiniCAST with diffusion flame and premixed flame Options : Generation of particles with high EC content in the size range 30 nm to 200 nm. *Aerosol Science and Technology, 53*(1), 29–44. https://doi.org/10.1080/02786826.2018.1536818

Fick, J., Pommer, L., Nilsson, C., & Andersson, B. (2003). Effect of OH radicals, relative humidity, and time on the composition of the products formed in the ozonolysis of α-pinene. *Atmospheric Environment, 37*(29), 4087–4096. https://doi.org/10.1016/S1352-2310(03)00522-3

George, I. J., Vlasenko, A., Slowik, J. G., Broekhuizen, K., & Abbatt, J. P. D. (2007). Heterogeneous oxidation of saturated organic aerosols by hydroxyl radicals: Uptake kinetics, condensed-phase products, and particle size change. *Atmospheric Chemistry and Physics, 7*(16), 4187–4201. https://doi.org/10.5194/acp-7-4187-2007

Gysel, M., Laborde, M., Olfert, J. S., Subramanian, R., & Gréhn, A. J. (2011). Effective density of Aquadag and fullerene soot black carbon reference materials used for SP2 calibration. *Atmospheric Measurement Techniques, 4*(12), 2851–2858. https://doi.org/10.5194/amt-4-2851-2011

Johnson, T. J., Irwin, M., Symonds, J. P. R., Olfert, J. S., & Boies, A. M. (2018). Measuring aerosol size distributions with the aerodynamic aerosol classifier. *Aerosol Science and Technology, 52*(6), 655–665. https://doi.org/10.1080/02786826.2018.1440063

Kang, E., Root, M. J., Toohey, D. W., & Brune, W. H. (2007). Introducing the concept of potential aerosol mass (PAM). *Atmospheric Chemistry and Physics, 7*, 5727–5744. https://doi.org/10.5194/acp-7-5727-2007

Keller, A., & Burtscher, H. (2012). A continuous photo-oxidation flow reactor for a defined measurement of the SOA formation potential of wood burning emissions. *Journal of Aerosol Science, 49*, 9–20. https://doi.org/10.1016/j.jaerosci.2012.02.007

Khalizov, A. F., Zhang, R., Zhang, D., Xue, H., Pagels, J., & McMurry, P. H. (2009). Formation of highly hygroscopic soot aerosols upon internal mixing with sulfuric acid vapor. *Journal of Geophysical Research Atmospheres, 114*(5), 1–15. https://doi.org/10.1029/2008JD010595

Kulkarni, P., Baron, P. A., Sorensen, C. M., & Harper, M. (2011). Nonspherical particle measurement: Shape factor, fractals, and fibers. In P. Kulkarni, P. A. Baron, & K. Willeke (Eds.), *Aerosol measurement: Principles, techniques, and applications* (pp. 509–547). John Wiley & Sons, Inc. https://doi.org/10.1002/9781118001684.ch23.

Lambe, A. T., Ahern, A. T., Williams, L. R., Slowik, J. G., Wong, J. P. S., Abbatt, J. P. D., et al. (2011). Characterization of aerosol photooxidation flow reactors: Heterogeneous oxidation, secondary organic aerosol formation and cloud condensation nuclei activity measurements. *Atmospheric Measurement Techniques, 4*(3), 445–461. https://doi.org/10.5194/amt-4-445-2011

Lambe, A. T., Ahern, A. T., Wright, J. P., Croasdale, D. R., Davidovits, P., & Onasch, T. B. (2015). Oxidative aging and cloud condensation nuclei activation of laboratory combustion soot. *Journal of Aerosol Science, 79*, 31–39. https://doi.org/10.1016/j.jaerosci.2014.10.001

Lambe, A. T., Cappa, C. D., Massoli, P., Onasch, T. B., Forestieri, S. D., Martin, A. T., et al. (2013). Relationship between oxidation level and optical properties of secondary organic aerosol. *Environmental Science and Technology, 47*(12), 6349–6357. https://doi.org/10.1021/es401043j

Lambe, A. T., Chhabra, P. S., Onasch, T. B., Brune, W. H., Hunter, J. F., Kroll, J. H., et al. (2015). Effect of oxidant concentration, exposure time, and seed particles on secondary organic aerosol chemical composition and yield. *Atmospheric Chemistry and Physics, 15*(6), 3063–3075. https://doi.org/10.5194/acp-15-3063-2015

Lambe, A. T., Onasch, T. B., Massoli, P., Croasdale, D. R., Wright, J. P., Ahern, A. T., et al. (2011). Laboratory studies of the chemical composition and cloud condensation nuclei (CCN) activity of secondary organic aerosol (SOA) and oxidized primary organic aerosol (OPOA). *Atmospheric Chemistry and Physics, 11*(17), 8913–8928. https://doi.org/10.5194/acp-11-8913-2011

Lefevre, G., Yon, J., Liu, F., & Coppallea, A. (2018). Spectrally resolved light extinction enhancement of coated soot particles. *Atmospheric Environment, 186*, 89–101. https://doi.org/10.1016/j.atmosenv.2018.05.029

Mader, B. T., Schauer, J. J., Seinfeld, J. H., Flagan, R. C., Yu, J. Z., Yang, H., et al. (2003). Sampling methods used for the collection of particle-phase organic and elemental carbon during ACE-Asia. *Atmospheric Environment, 37*(11), 1435–1449. https://doi.org/10.1016/S1352-2310(02)01061-0

McMurry, P. H. (2000). A review of atmospheric aerosol measurements. *Atmospheric Environment, 34*(12–14), 1959–1999. https://doi.org/10.1016/S1352-2310(99)00455-0

Moallemi, A., Kazemimanesh, M., Corbin, J. C., Thomson, K., Smallwood, G., Olfert, J. S., et al. (2019). Characterization of black carbon particles generated by a propane-fueled miniature inverted soot generator. *Journal of Aerosol Science, 135*(June), 46–57. https://doi.org/10.1016/j.jaerosci.2019.05.004

Moffet, R. C., & Prather, K. A. (2009). In-situ measurements of the mixing state and optical properties of soot with implications for radiative forcing estimates. *Proceedings of the National Academy of Sciences of the United States of America, 106*(29), 11872–11877. https://doi.org/10.1073/pnas.0900040106

Molteni, U., Bianchi, F., Klein, F., Haddad, I. El, Frege, C., Rossi, M. J., et al. (2018). *Formation of highly oxygenated organic molecules from aromatic compounds*.

Müller, T., Henzing, J. S., De Leeuw, G., Wiedensohler, A., Alastuey, A., Angelov, H., et al. (2011). Characterization and intercomparison of aerosol absorption photometers: Result of two intercomparison workshops. *Atmospheric Measurement Techniques, 4*, 245–268. https://doi.org/10.5194/amt-4-245-2011

Nakayama, T., Suzuki, H., Kagamitani, S., & Ikeda, Y. (2015). Characterization of a three wavelength photoacoustic soot spectrometer (PASS-3) and a photoacoustic extinctiometer (PAX). *Journal of the Meteorological Society of Japan, 93*(2), 285–308. https://doi.org/10.2151/jmsj.2015-016

Nishida, R. T., Johnson, T. J., Boies, A. M., & Hochgreb, S. (2019). Measuring aerosol active surface area by direct ultraviolet photoionization and charge capture in continuous flow. *Aerosol Science and Technology, 53*(12), 1429–1440. https://doi.org/10.1080/02786826.2019.1661958

Ogren, J. A., & Charlson, R. J. (1983). Elemental carbon in the atmosphere: Cycle and lifetime. *Tellus B: Chemical and Physical Meteorology, 35 B*(4), 241–254. https://doi.org/10.1111/j.1600-0889.1983.tb00027.x

Pei, X., Hallquist, M., Eriksson, A. C., Pagels, J., Donahue, N. M., Mentel, T., et al. (2018). Morphological transformation of soot: Investigation of microphysical processes during the condensation of sulfuric acid and limonene ozonolysis product vapors. *Atmospheric Chemistry and Physics, 18*(13), 9845–9860. https://doi.org/10.5194/acp-18-9845-2018

Penner, J. E., Andreae, M. O., Annegarn, H., Barrie, L., Feichter, J., Hegg, D., et al. (2001). Aerosols, their direct and indirect effects. In M. N. Houghton, J. T. Y. Ding, D. J. Griggs, C. A. J. P. J. van der Linden, X. Dai, & K. Maskell (Eds.), *IPCC third assessment report: Climate change 2001: The scientific basis* (Vol. 5, pp. 289–348). Cambridge UK and New York USA: Cambridge University Press. https://doi.org/10.1029/JD091iD01p01089.

Petzold, A., Ogren, J. A., Fiebig, M., Laj, P., Li, S.-M. M., Baltensperger, U., et al. (2013). Recommendations for reporting "black carbon" measurements. *Atmospheric Chemistry and Physics, 13*(16), 8365–8379. https://doi.org/10.5194/acp-13-8365-2013

Pospisilova, V., Lopez-Hilfiker, F. D., Bell, D. M., Haddad, I. El, Mohr, C., Huang, W., et al. (2020). On the fate of oxygenated organic molecules in atmospheric aerosol particles. *Science Advances, 6*(11), 1–12. https://doi.org/10.1126/sciadv.aax8922

Rissler, J., Nordin, E. Z., Eriksson, A. C., Nilsson, P. T., Frosch, M., Sporre, M. K., et al. (2014). Effective density and mixing state of aerosol particles in a near-traffic urban environment. *Environmental Science and Technology, 48*, 6300–6308. https://doi.org/10.1021/es5000353

Saathoff, H., Naumann, K.-H. H., Schnaiter, M., Schöck, W., Möhler, O., Schurath, U., et al. (2003a). Coating of soot and (NH4)2SO4 particles by ozonolysis products of α-pinene. *Journal of Aerosol Science, 34*(10), 1297–1321. https://doi.org/10.1016/S0021-8502(03)00364-1

Saathoff, H., Naumann, K.-H. H., Schnaiter, M., Schöck, W., Möhler, O., Schurath, U., et al. (2003b). Coating of soot and (NH4)2SO4particles by ozonolysis products of α-pinene. *Journal of Aerosol Science, 34*(10), 1297–1321. https://doi.org/10.1016/S0021-8502(03)00364-1

Saleh, R., Cheng, Z., & Atwi, K. (2018). The Brown-black continuum of light-absorbing combustion aerosols. *Environmental Science and Technology Letters, 5*(8), 508–513. https://doi.org/10.1021/acs.estlett.8b00305

Schmid, O., Artaxo, P., Arnott, W. P., Chand, D., Gatti, L. V., Frank, G. P., et al. (2006). Spectral light absorption by ambient aerosols influenced by biomass burning in the amazon basin . I : Comparison and field calibration of absorption measurement techniques. *Atmospheric Chemistry and Physics, 6*(5), 3443–3462. https://doi.org/10.5194/acpd-5-9355-2005

Schnaiter, M., Linke, C., Möhler, O., Naumann, K. H., Saathoff, H., Wagner, R., et al. (2005). Absorption amplification of black carbon internally mixed with secondary organic aerosol. *Journal of Geophysical Research - D: Atmospheres, 110*(19), 1–11. https://doi.org/10.1029/2005JD006046

Simon, M., Dada, L., Heinritzi, M., Scholz, W., Stolzenburg, D., Fischer, L., et al. (2020). Molecular understanding of new-particle formation from α-pinene between −50 and +25 °C. *Atmospheric Chemistry and Physics, 20*, 9183–9207. https://doi.org/10.5194/acp-20-9183-2020

Tavakoli, F., & Olfert, J. S. (2014). Determination of particle mass, effective density, mass-mobility exponent, and dynamic shape factor using an aerodynamic aerosol classifier and a differential mobility analyzer in tandem. *Journal of Aerosol Science, 75*, 35–42. https://doi.org/10.1016/j.jaerosci.2014.04.010

Tillmann, R., Hallquist, M., Jonsson, Å. M., Kiendler-Scharr, A., Saathoff, H., Iinuma, Y., et al. (2010). Influence of relative humidity and temperature on the production of pinonaldehyde and OH radicals from the ozonolysis of α-pinene. *Atmospheric Chemistry and Physics, 10*(15), 7057–7072. https://doi.org/10.5194/acp-10-7057-2010

Virkkula, A. (2010). Correction of the calibration of the 3-wavelength particle soot absorption photometer (3 λ PSAP). *Aerosol Science and Technology, 44*(8), 706–712. https://doi.org/10.1080/02786826.2010.482110

Vivanco, M. G., Santiago, M., Martínez-Tarifa, A., Borrás, E., Ródenas, M., García-Diego, C., et al. (2011). SOA formation in a photoreactor from a mixture of organic gases and HONO for different experimental conditions. *Atmospheric Environment, 45*(3), 708–715. https://doi.org/10.1016/j.atmosenv.2010.09.059

Wang, Y., Liu, F., He, C., Bi, L., Cheng, T., Wang, Z., et al. (2017). Fractal dimensions and mixing structures of soot particles during atmospheric processing. *Environmental Science and Technology Letters, 4*(11), 487–493. https://doi.org/10.1021/acs.estlett.7b00418

Weingartner, E., Baltensperger, U., & Burtscher, H. (1995). Growth and structural change of combustion aerosols at high relative humidity. *Environmental Science and Technology, 29*(12), 2982–2986. https://doi.org/10.1021/es00012a014

Weingartner, E., Burtscher, H., & Baltensperger, U. (1997). Hygroscopic properties of carbon and diesel soot particles. *Atmospheric Environment, 31*(15), 2311–2327. https://doi.org/10.1016/S1352-2310(97)00023-X

Weingartner, E., Saathoff, H., Schnaiter, M., Streit, N., Bitnar, B., & Baltensperger, U. (2003). Absorption of light by soot particles: Determination of the absorption coefficient by means of aethalometers. *Journal of Aerosol Science, 34*(10), 1445–1463. https://doi.org/10.1016/S0021-8502(03)00359-8

Wyche, K. P., Monks, P. S., Ellis, A. M., Cordell, R. L., Parker, A. E., Whyte, C., et al. (2009). Gas phase precursors to anthropogenic secondary organic aerosol : Detailed observations of 1 , 3 , 5-trimethylbenzene photooxidation. *Atmospheric Chemistry and Physics, 9*, 635–665.

Yuan, J., Modini, R. L., Zanatta, M., Herber, A., Müller, T., Wehner, B., et al. (2020). Variability in the mass absorption cross-section of black carbon (BC) aerosols is driven by BC internal mixing state at a central European background site (Melpitz, Germany) in winter. *Atmospheric Chemistry and Physics*, (January), 1–36. https://doi.org/10.5194/acp-2020-41

Zhang, R., Khalizov, A. F., Pagels, J., Zhang, D., Xue, H., & McMurry, P. H. (2008). Variability in morphology, hygroscopicity, and optical properties of soot aerosols during atmospheric processing. *Proceedings Of the National Academy Of Sciences Of the United States of America, 105*(30), 10291–10296. https://doi.org/10.1073/pnas.0804860105

Zhang, X., Mcvay, R. C., Huang, D. D., Dalleska, N. F., Aumont, B., Flagan, R. C., et al. (2015). Formation and evolution of molecular products in α -pinene secondary organic aerosol. *Proceedings of the National Academy of Sciences, 112*(46), 14168–14173. https://doi.org/10.1073/pnas.1517742112

Zhang, G., Peng, L., Lian, X., Lin, Q., Bi, X., Chen, D., et al. (2018). An improved absorption Ångström exponent (AAE)-Based method for evaluating the contribution of light absorption from Brown carbon with a high-time resolution. *Aerosol and Air Quality Research, 19*, 15–24. https://doi.org/10.4209/aaqr.2017.12.0566

Zhou, Y., Zhang, H., Parikh, H. M., Chen, E. H., Rattanavaraha, W., Rosen, E. P., et al. (2011). Secondary organic aerosol formation from xylenes and mixtures of toluene and xylenes in an atmospheric urban hydrocarbon mixture: Water and particle seed effects (II). *Atmospheric Environment, 45*(23), 3882–3890. https://doi.org/10.1016/j.atmosenv.2010.12.048